Journal of Statistical Physics, Vol. 107, Nos. 1/2, April 2002 (© 2002)

On Implementation of Boundary Conditions in the Application of Finite Volume Lattice Boltzmann Method

Y. T. Chew,[1] C. Shu,[1] and Y. Peng[1, 2]

Received February 13, 2001; accepted September 3, 2001

A new implementation of boundary condition based on the half-covolume and bounce-back rule for the non-equilibrium distribution function for the finite volume LBM is proposed here. The numerical simulation results for the expansion channel flow and driven cavity problem indicate that this method is workable for arbitrary meshes. In addition, the fourth order Runge–Kutta scheme is found to be a practical way in the LBM to accelerate the calculation speed.

KEY WORDS: Lattice-Boltzmann equation; finite volume; boundary conditions; half covolume scheme; bounce back.

1. INTRODUCTION

In recent years, the LBM has been developed into an alternative useful tool to solve complex fluid flows. Although it has notable advantages over the conventional methods, there are still some limitations in the implementation of LBM models. One of these is that the LBM scheme on a Cartesian-like grid is restricted to a special class of uniform and regular spatial lattices. Some workers have attempted to extend the applicability to the irregular lattices. Succi[1, 2] was the first to propose a finite-volume formulation of the LBM. However, the empirical formulae used are quite complicated even for the simple rectangular meshes, and a free parameter has to be introduced and adjusted in order to minimize the numerical diffusion. To improve it, Chen[3] developed another finite-volume scheme. With properly chosen forms of the state-flux functions, both exact conservation laws and equilibrium balance conditions are achieved as in the original LBM. In the

[1] Department of Mechanical Engineering National University of Singapore, Singapore 119260.
[2] To whom correspondence should be addressed; e-mail: engp9343@nus.edu.sg

0022-4715/02/0400-0539/0 © 2002 Plenum Publishing Corporation

new method proposed by He, Luo and Dembo,[4] an interpolation step is introduced after stream and collision steps to determine the density distributions at the grid points for the next time step. Filippova and Hanel[5] presented the multiscale LBM scheme with the boundary-fitting formulation on the curvilinear boundaries. It uses the concept of hierarchical grid refinement. The calculation is based on a coarse grid covering the whole integration domain. In a critical region, a finer grid is superposed to the basic grid. The calculation proceeds with large time-step according to the coarse grid; while on the finer grids, several time steps according to the refinement ratio are performed to advance to the same time level. This feature is very important for the computations of time-dependent flows. For the computation of steady-state incompressible flows, the use of several smaller time-steps on the fine grid will increase the computational time. In order to remove this drawback, the use of smaller amount of time steps on the fine grid is proposed. For the time-dependent computation, this is connected with the change of "molecular" speeds[6] on the fine grid so that the temporal accuracy will not be impaired in certain limits. For steady-state computation, the saving of CPU time can be even larger, since the same amount of time steps can be chosen on coarse and fine grids as well. Recently, a new method is proposed by Xi,[7–10] which can be used on irregular meshes with arbitrary connectivity. It is based on modern finite-volume methods[11] and keeps the simplicity of the conventional LBM.

The main focus associated with this new scheme is the implementation of the boundary conditions. The half-covolume technique is introduced and used by Peng and Xi[12] at the solid boundary. This method is quite general and simple in the sense that it does not assume the fluid properties and the orientations of the boundary walls. It is very robust when the inlet and outlet boundaries are periodical. However, it will cause some problems when it is used in other flow problems such as the velocity profile being given at the inlet. In order to solve this problem, a new implementation of boundary condition based on the half-covolume and bounce-back rule for the non-equilibrium distribution function for the finite volume LBM is proposed here. Besides, this problem is more severe at the corner points. In driven cavity problem, the left bottom small vortex cannot be obtained when no special treatment is used at the corner points. So some additional treatments are used at the corner nodes. As will be shown in Section 3.2, the physical background of bounce back rule is the compliance of Grad's thirteen-moments.[13] When the compliance of Grad's thirteen-moments or the bounce back rule is broken, the no-slip boundary condition on the solid wall may not be guaranteed. Considering the fact that both the complete bounce back scheme[14] and half-covolume technique do not distinguish among distribution functions, the combination of the half-covolume and

the bounce back scheme are very easy to implement in a computer code. The proposed approach is validated by its application to solve the 2D expansion channel flow and the driven cavity flow.

2. THE FINITE-VOLUME LBM MODEL

The finite-volume approach starts with the lattice Boltzmann equation in differential form, which reads:

$$\frac{\partial f_i}{\partial t} + v_i \bullet \nabla f_i = \Omega_i + \alpha v_i \bullet \mathrm{F} \tag{1}$$

where

$$\Omega_i = -\frac{1}{\tau}\left[f_i(x, v_i, t) - f_i^{\mathrm{eq}}(x, v_i, t)\right]$$

$$f_i^{\mathrm{eq}} = w_i \rho \left[1 + \frac{3v_i \bullet u}{c^2} + \frac{9(v_i \bullet u)^2}{2c^2} - \frac{3u^2}{2c^2}\right]$$

$$v_i = \begin{cases} 0 & i = 0 \\ (\cos[(i-1)\,\pi/2],\ \sin[(i-1)\,\pi/2])\,c & i = 1\text{–}4 \\ \sqrt{2}\,(\cos[(i-5)\,\pi/2+\pi/4],\ \sin[(i-5)\,\pi/2+\pi/4])\,c & i = 5\text{–}8 \end{cases}$$

$$w_0 = 4/9, \qquad w_i = 1/9 \quad \text{for } i = 1\text{–}4 \qquad \text{and} \qquad w_i = 1/36 \quad \text{for } i = 5\text{–}8$$

$$\alpha = 1 \Big/ \sum_i v_{ix}^2 = 1 \Big/ \sum_i v_{iy}^2$$

Figure 1 shows a finite element surrounding an interior node P. Here P, P_1 to P_8 are the grid points. A to H represent the edges of the control volume over which integration of the PDE is performed. A, C, E, and G are the midpoints of the edge PP_1, PP_3, PP_5 and PP_7 respectively. B, D, F, and H are the geometric center of element $PP_1P_2P_3$, $PP_3P_4P_5$, $PP_5P_6P_7$ and $PP_7P_8P_1$ respectively.

The cell-vertex type is used here. In this type of formulation, all the density distribution functions at the grid nodes are known while the distribution functions at other locations are interpolated from the known values at the grid points using standard interpolation technique.

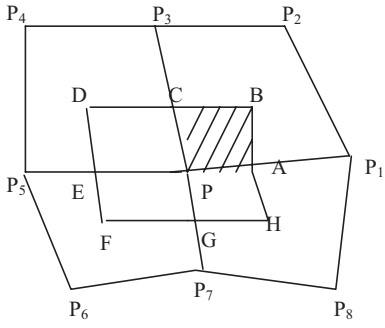

Fig. 1. Diagram of a finite element surrounding an interior node P.

The integration of the first term in Eq. (1) is approximated as

$$\int_{\mathrm{PABC}} \frac{\partial f_i}{\partial t}\, d\sigma = \frac{\partial f_i(\mathrm{P})}{\partial t}\, s_{\mathrm{PABC}} \tag{2}$$

where s_{PABC} is the area of PABC and $f_i(\mathrm{P})$ is the f_i value at grid point P. In what follows, the grid-node index is given in parentheses following the f_i values. In the above equation, an approximation that f_i is constant over the area PABC is used to prevent solving a set of equations.

The integration of the second term of Eq. (1) will give fluxes through the four edges PA, AB, BC, and CP. Since the summation over all the polygons like PABC, PCDE, PEFG, and PGHA will be done, the net flux through internal edges (PA, PC, PE, PG) will cancel out. Therefore, the explicit expression for the internal edges will be omitted. That is

$$\int_{\mathrm{PABC}} v_i \bullet \nabla f_i\, d\sigma = v_i \bullet \int_{AB} f_i\, dl + v_i \bullet \int_{BC} f_i\, dl + I_s \tag{3}$$

where I_s represents fluxes through internal edges. With the standard assumption of bilinearity of f_i in quadrilateral elements, the flux is then given by

$$\begin{aligned}\int_{\mathrm{PABC}} v_i \bullet \nabla f_i\, d\sigma &= v_i \bullet n_{\mathrm{AB}} l_{\mathrm{AB}} [f_i(\mathrm{A}) + f_i(\mathrm{B})]/2 \\ &= v_i \bullet n_{\mathrm{BC}} l_{\mathrm{BC}} [f_i(\mathrm{B}) + f_i(\mathrm{C})]/2 + I_s \end{aligned} \tag{4}$$

where n_{AB} and n_{BC} are the unit vectors normal to the edge AB and BC, respectively, and l_{AB} and l_{BC} are the lengths of AB and BC, respectively.

With the assumption of bi-linearity of f_i and f_i^{eq} over the quadrilateral elements, the integration over the collision term of Eq. (1) results in the following formula:

$$-\int_{PABC} \frac{1}{\tau}(f_i - f_i^{eq})\, d\sigma = -\frac{s_{PABC}}{\tau}[\Delta f_i(P) + \Delta f_i(A) + \Delta f_i(B) + \Delta f_i(C)]/4 \tag{5}$$

where

$$\Delta f_i(P) = f_i(P) - f_i^{eq}(P)$$
$$\Delta f_i(A) = f_i(A) - f_i^{eq}(A)$$
$$\Delta f_i(B) = f_i(B) - f_i^{eq}(B)$$
$$\Delta f_i(C) = f_i(C) - f_i^{eq}(C)$$

Here $f_i(A)$, $f_i(B)$, $f_i(C)$ and their corresponding equilibrium particle distribution functions $f_i^{eq}(A)$, $f_i^{eq}(B)$, $f_i^{eq}(C)$ are the values at non-grid nodes A, B, and C, respectively. This may be obtained by interpolation from the four grid nodes at element $PP_1P_2P_3$,

$$f_i(A) = [f_i(P) + f_i(P_1)]/2$$
$$f_i(B) = [f_i(P) + f_i(P_1) + f_i(P_2) + f_i(P_3)]/4$$
$$f_i(C) = [f_i(P) + f_i(P_3)]/2$$
$$f_i^{eq}(A) = [f_i^{eq}(P) + f_i^{eq}(P_1)]/2$$
$$f_i^{eq}(B) = [f_i^{eq}(P) + f_i^{eq}(P_1) + f_i^{eq}(P_2) + f_i^{eq}(P_3)]/4$$
$$f_i^{eq}(C) = [f_i^{eq}(P) + f_i^{eq}(P_3)]/2$$

With these results, the integration of Eq. (1) over the polygon PABC is complete. The integration over the whole control volume ABCDEFGH is just the sum of contributions from all these terms over different polygons PABC, PCDE, PEFG, and PGHA. Therefore, f_i at grid node P is updated as follows:

$$f_i(P, t+\Delta t) = f_i(P, t) + \frac{\Delta t}{s_P}\left(\sum_{\text{around P}} (\text{collisions}) - \sum_{\text{around P}} (\text{fluxes})\right) + \alpha v_i \bullet F \tag{6}$$

where s_P is the total area of the control volume around grid node P, and "collisions" and "fluxes" refer, respectively, to the finite-volume-integrated contributions from the collision term and fluxes.

3. IMPLEMENTATION OF BOUNDARY CONDITIONS

3.1. Half-Covolume Scheme

Let P, P_5, and P_1 are boundary nodes separating the fluid (upper half) from the lower half. As for the interior fluid nodes, the value of f_i at P is updated through Eq. (6) by covolume integrals. At the boundary, the covolume is not complete in the 2π direction as the polygons PEFG and PGHA are not included. This leads to the difference when integrating the second term of Eq. (1) over polygons PABC and PCDE. The flux terms over the edges PA and EP, which are omitted in the case of interior nodes, must be included in the calculation. They are actually easy to evaluate by Eq. (4). The velocity of the boundary wall is used when f_i^{eq} for the boundary nodes are calculated in order to enforce the no-slip boundary condition. This is an effective way to implement the boundary condition for the fluid problems where the inlet and outlet are periodic conditions. This can be verified by the following cases.

(1) Two-dimensional Poiseuille flow between two parallel plates.

The external force is $F = 2.604 \times 10^{-5}\mathbf{e}_x$. The total 64×32 mesh points are used. The analytical solution for the case is $u_x(y) = FL^2/(8\rho\upsilon)\lfloor 1-(2y/L-1)^2\rfloor$, where L is the channel width. Figure 2 shows the numerical results with the analytical solution. It can be seen that the agreement is excellent.

(2) Two-dimensional rotating Couette flow between two concentric cylinders.

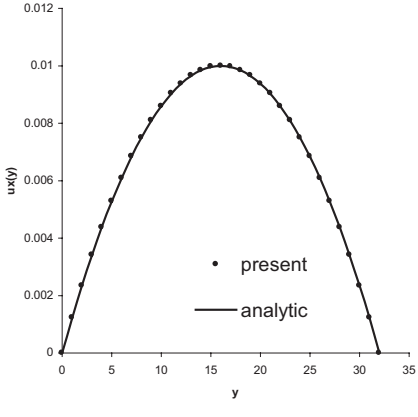

Fig. 2. Numerical velocity profile for the Poiseuille flow as compared with analytic solution.

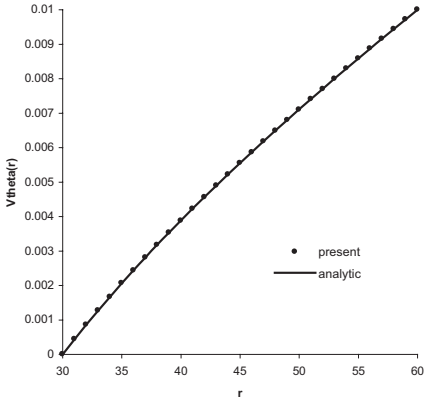

Fig. 3. Numerical velocity profile for rotating Couette flow as compared with analytic solution.

The outer cylinder rotates with velocity $V\mathbf{e}_\theta$, while the inner cylinder is stationary. In this simulation, the radii of the two cylinders are $R_1 = 30$ and $R_2 = 60$, the velocity $V = 0.01$. The 180×30 mesh points are used. The analytical solution for the problem is $u_\theta(r) = (V_2 R_2 r - \frac{V_2 R_1^2 R_2}{r})/(R_2^2 - R_1^2)$. Figure 3 shows the numerical result of the steady velocity profile and the corresponding analytical solution. One can see from Fig. 3 that the agreement is also excellent.

(3) Plane Couette flow with a half-cylinder of radius R resting on the bottom plane.

The meshes are generated using elliptic grid generation method as shown in Fig. 4. In this simulation, $R = 20$ is for the radius of cylinder,

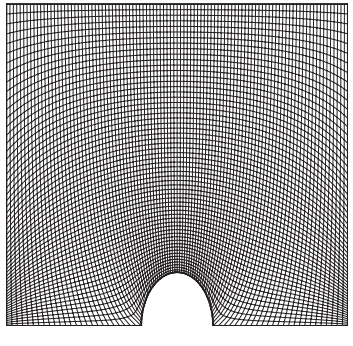

Fig. 4. Meshes used for flow past a half-cylinder resting on a plane.

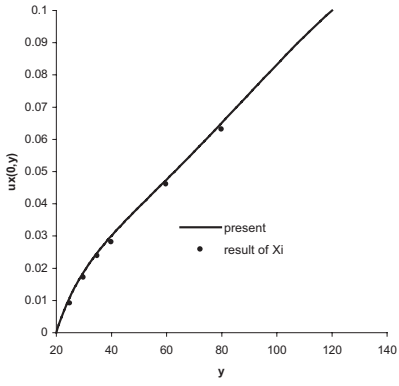

Fig. 5. Velocity field u in the center ($x = 0$) of the channel for flow past a half-cylinder resting on a plane.

$U = 0.1$ is for the top plane speed, and the plane is $9.5R \times 6R$. The mesh size used is 100×60. Figure 5 shows the velocity profile across y in the center of the channel. Good agreement between present results and those given by Xi[8] was found.

3.2. Half-Covolume plus Bounce Back Method

It was found from the above section that half covolume method is very effective in solving flow problems where the inlet and outlet are periodical. However, it would cause some problems when it is used in other cases such as the velocity profile being given at the inlet. The reason for this may lie in the inconsistency with Grad's 13 moments expansion, which is needed to be satisfied for a robust and efficient boundary condition.

According to Grad's "13-moment" system, the non-equilibrium density distribution function can be written as

$$f^{\text{neq}} = f^{\text{eq}}\left(\frac{\Pi : (v_i - u)(v_i - u)}{2pRT} - \frac{S \cdot (v_i - u)}{2pRT}\left(1 - \frac{(v_i - u)^2}{(D+2)\,RT}\right)\right) \tag{7}$$

where Π and S are the stress tensor and heat flux vector, respectively. The terms involving $O(u)$ and higher order can be neglected since the non-equilibrium distribution itself is very small, which leads to

$$f^{\text{neq}} = f^{\text{eq}}\left(\frac{\Pi : v_i v_i}{2(RT)^2} - \frac{S \cdot v_i}{2(RT)^2}\left(1 - \frac{v_i^2}{(D+2)\,RT}\right)\right) \tag{8}$$

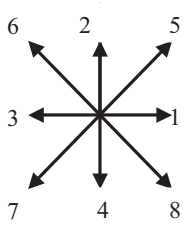

Fig. 6. Schematic plot of velocity directions of the 2-D model at the bottom wall.

For the isothermal flow, the heat transfer term can be neglected, and then it can be approximated by

$$f^{\text{neq}} = f^{\text{eq}} \frac{\Pi : v_i v_i}{2(RT)^2} \tag{9}$$

So

$$f_{\alpha}^{\text{neq, iso}} = f_{\beta}^{\text{neq, iso}} \tag{10}$$

where α and β have the opposite direction.

On the solid wall, Eq. (10) is actually the bounce back condition. This implies that the physical background of bounce back rule is the compliance of Grad's thirteen-moments. In the following applications, we combine the half-covolume and the bounce back rule for the non-equilibrium distribution to implement the boundary condition. As an example, we consider the case of the bottom wall. The nine-bit model is shown in Fig. 6. For the bottom wall, the distribution at direction 7, 4, and 8 are determined by half-covolume, and the distribution at direction 5, 2, and 6 are determined by the bounce back rule for the non-equilibrium distribution through Eq. (10).

To test the validity of this new implementation of the boundary condition, the numerical simulations for the expansion channel flow are carried out. This problem has been chosen by a workshop of International Association for Hydraulic Research (IAHR) working group (Napolitano *et al.*, 1985)[15] as a suitable test case for assessing the capabilities of the current numerical methods on refined modeling of the flows on the subject of computing laminar flows in complex geometry. The total length of the channel is chosen to be Re/3. The lower boundary (solid wall) of the channel is given by the following expression:

$$y_l(x) = \frac{1}{2}\left[\tanh\left(2 - \frac{30 \cdot x}{\text{Re}}\right) - \tanh(2) \right] \tag{11}$$

At the inlet, the velocity profile is given as

$$\begin{cases} u = 1.5 \times (2y - y^2) \\ v = 0 \end{cases} \quad \text{for} \quad x = 0, \quad 0 \leqslant y \leqslant 1 \tag{12}$$

The velocity boundary condition produced by Zou and He[14] is used here at the inlet.

The mesh size used for this simulation is 71×31. Figures 7 and 8 show the wall vorticity distribution for $\mathrm{Re} = 10$ and $\mathrm{Re} = 100$. The present results compare well with the benchmark solution of IAHR workshop (Napolitano *et al.*, 1985) given by Cliffe *et al.* using a finite element method with results being grid-independent. Figure 9 displays the wall vorticity distribution for different Reynolds numbers calculated by the present method. It is confirmed in this figure that as Reynolds number increases to the value of much larger than 1, the solution takes on a quasi-self-similar form, i.e., the wall vorticity becomes independent of Re when plotted vs. x/x_{out}. Figure 10 shows the streamlines for $\mathrm{Re} = 10$. The separation region is shown clearly in this figure.

The above numerical results show that the new boundary method is valid for solving the flow problem with complex geometry of boundaries.

3.3. Special Treatment on the Corner Points

For some flow problems, which have the corner points such as driven cavity problem, the implementation of the boundary condition at the

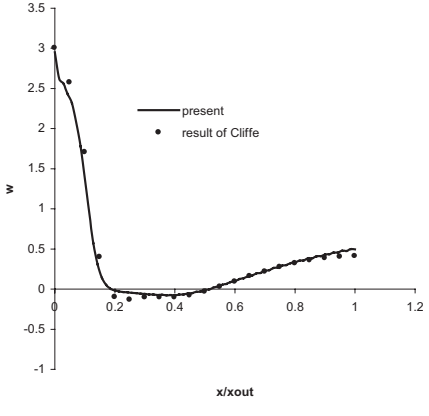

Fig. 7. Wall vorticity distribution for expansion channel flow at $\mathrm{Re} = 10$.

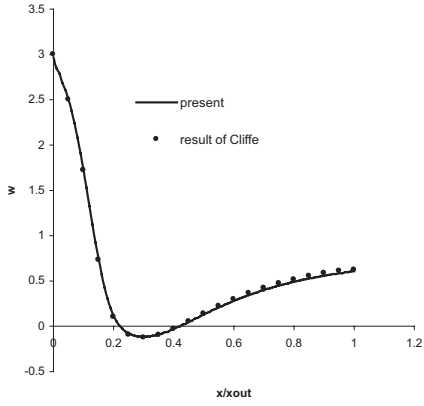

Fig. 8. Wall vorticity distribution for expansion channel flow at Re = 100.

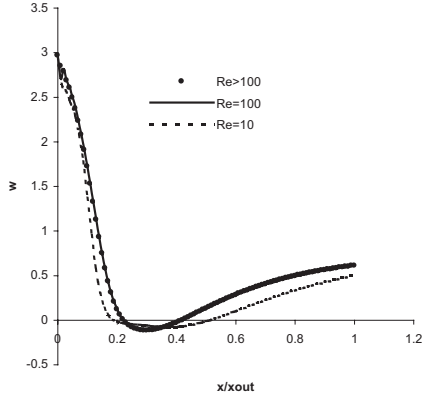

Fig. 9. Wall vorticity distribution for expansion channel flow at different Reynolds numbers.

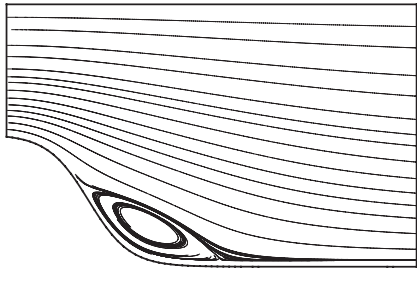

Fig. 10. Streamline for expansion channel flow at Re = 10.

corner points is very important. At the corner points, the velocity directions of the 2-D model are show in Fig. 11. For the direction 6 and direction 8, the values for these two directions have little influence on the results of the numerical simulation using the original LBM, because they do not contribute any information into the interior parts. But for finite volume LBM, these values will be used when calculating the interior points at these two directions. So it is very crucial for the choice of the values at these two directions. Take the case of driven cavity problem as an example. At $\mathrm{Re}=100$, the values of the equilibrium function were given for the distribution functions at these two directions at the beginning. The primary and the right bottom vortices can be captured correctly and the left bottom small vortex cannot be obtained. This means that the equilibrium boundary condition does not have enough accuracy for the complex flow pattern. The left bottom small vortex is plagued by the numerical errors. In order to increase the accuracy, the first order extrapolation scheme at these two directions was tried. At these two directions, the values are obtained by extrapolation from the two interior points, and for other directions, the half-covolume combined with the bounce back method are used. The numerical results of this treatment are very accurate. The results for $\mathrm{Re}=100$ are shown in Figs. 12–15. The mesh size used for these results is 101×101.

According to the present study, for $\mathrm{Re}=100$, the center of the primary vortex is at $x=0.617$, $y=0.737$, the center of the left corner vortex is at $x=0.030$, $y=0.037$, and the center of the right corner vortex is at $x=0.0945$, $y=0.060$. The results are in good agreement with those by Ghia *et al.*[16] (for $\mathrm{Re}=100$ by Ghia *et al.*, $x=0.6172$, $y=0.7344$ for the primary vortex, $x=0.0313$, $y=0.0391$ for the left corner vortex, and $x=0.9453$, $y=0.0625$ for the right corner vortex.).

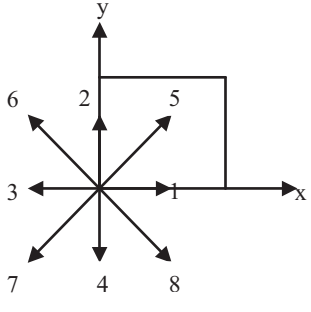

Fig. 11. Schematic plot of velocity directions of 2-D model at the left-bottom conner point.

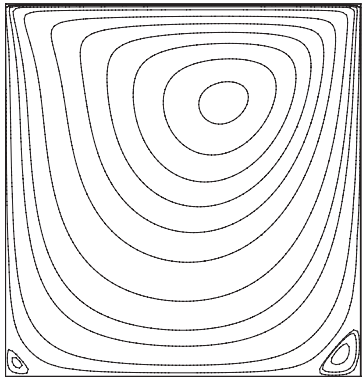

Fig. 12. Streamlines for driven cavity flow at Re = 100.

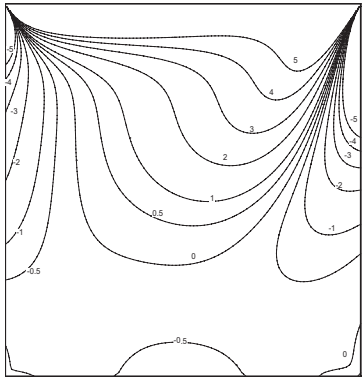

Fig. 13. Vorticity contours for driven cavity flow at Re = 100.

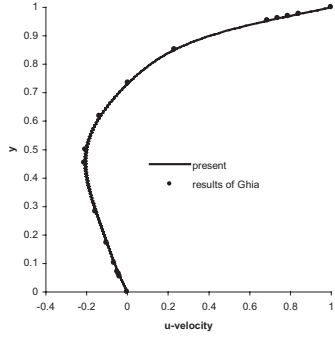

Fig. 14. Comparison of *u*-velocity profiles along the vertical centerline of driven cavity at Re = 100.

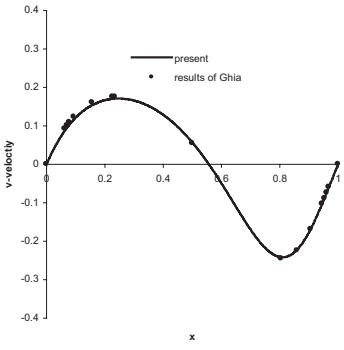

Fig. 15. Comparison of v-velocity profiles along the horizontal centerline of driven cavity at $\mathrm{Re}=100$.

To further validate the present method, numerical computations were performed for $\mathrm{Re}=400$ and $\mathrm{Re}=1000$, and the results are shown in Figs. 16–19. The mesh sizes used for $\mathrm{Re}=400$ and $\mathrm{Re}=1000$ are respectively 201×201 and 251×251. Clearly, a much larger number of mesh points is needed for $\mathrm{Re}=400$ and 1000 in order to obtain accurate numerical results. This may be one of the shortcomings of the finite volume LBM for simulation of flows with high Reynolds number. In this paper, we aim to improve the implementation of boundary conditions rather than the finite volume LBM itself. Our numerical results for the driven cavity problem showed that the special treatment on the corner points is needed and effective.

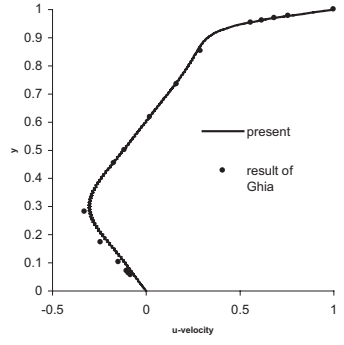

Fig. 16. Comparison of u-velocity profiles along the vertical centerline of driven cavity at $\mathrm{Re}=400$.

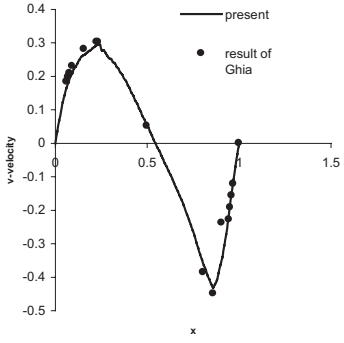

Fig. 17. Comparison of v-velocity profiles along the horizontal centerline of driven cavity at $\mathrm{Re} = 400$.

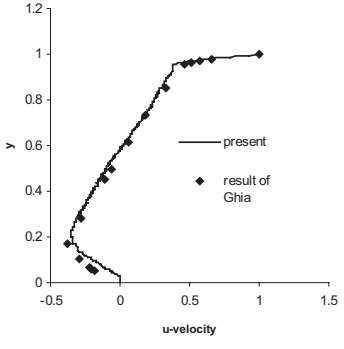

Fig. 18. Comparison of u-velocity profiles along the vertical centerline of driven cavity at $\mathrm{Re} = 1000$.

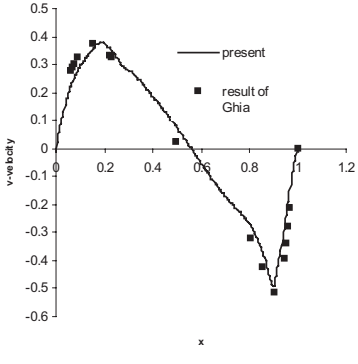

Fig. 19. Comparison of v-velocity profiles along the horizontal centerline of driven cavity at $\mathrm{Re} = 1000$.

3.4. The Fourth Order Runge–Kutta Scheme

In order to accelerate the calculation speed, the fourth order Runge–Kutta scheme is used in this work. The general mth order Runge–Kutta scheme can be written as

$$f^{(0)} = f^{(n)} \tag{13a}$$

$$f^{(k)} = f^{(0)} + \alpha_k \, \Delta f^{(k-1)}, \qquad k = 1,\ldots, m \tag{13b}$$

$$f^{(n+1)} = f^{(m)} \tag{13c}$$

where

$$\Delta f^{(k-1)} = \frac{\Delta t}{s_P}\left(\sum_{\text{around } P} \text{collisions}(f^{(k-1)}) - \sum_{\text{around } P} \text{fluxes}(f^{(k-1)}) \right)$$

When m is taken as 4, we can get the fourth order Runge–Kutta scheme, in which the coefficients are taken as

$$\alpha_1 = 0.0833, \qquad \alpha_2 = 0.2069, \qquad \alpha_3 = 0.4265, \qquad \alpha_4 = 1$$

To test the efficiency of the Runge–Kutta scheme, we performed numerical integration in the time direction by two schemes: Euler explicit scheme and the fourth order Runge–Kutta scheme. Two cases were studied. The first case is the expansion channel flow. The Reynolds number is taken as 10 and the mesh size is 71×31. The convergence criterion is set to

$$\sum_{i,j} |\sqrt{(u_{i,j}^2 + v_{i,j}^2)^{n+1}} - \sqrt{(u_{i,j}^2 + v_{i,j}^2)^{n}}| \Big/ \sum_{i,j} |\sqrt{(u_{i,j}^2 + v_{i,j}^2)^{n}}| \leqslant 10^{-6} \tag{14}$$

where n is the time level. It was found that the time step for the fourth order Runge–Kutta scheme can be taken as 6.5 times greater than that for the Euler explicit scheme. The second case is the driven cavity flow. The Reynolds number is taken as 100 and the mesh size is chosen as 101×101. The convergence criterion is set the same as in the first case. For this case, the time step of the fourth order Runge–Kutta scheme can be 5 times larger than that of the Euler explicit scheme. For both cases, the overall CPU time required by the fourth order Runge–Kutta scheme on Compaq ES40 workstation is less than that by the Euler explicit scheme. But the Euler explicit scheme requires less virtual storage as compared to the fourth order Runge–Kutta scheme. The CPU time (s) and the memory required by Euler explicit scheme and the fourth order Runge–Kutta scheme for simulation of expansion channel flow and the lid driven cavity flow are shown in Table I.

Table I. Comparison of CPU Time and Memory Between Euler Explicit Scheme and Fourth Order Runge–Kutta Scheme

		Euler explicit		4th order Runge–Kutta	
Problem	Mesh size	CPU time (seconds)	Memory (MB)	CPU time (seconds)	Memory (MB)
Expansion channel flow	71×31	485.10	11	336.25	12
Driven cavity flow	101×101	1658.51	15	1219.42	19

4. CONCLUSION

A new implementation of boundary conditions for the finite volume LBM has been developed in this paper. It is based on the half-covolume and the bounce-back rule for the non-equilibrium distribution function. For the test problems of expansion channel flow and driven cavity flow, good results can be obtained using this new approach.

The fourth order Runge–Kutta integration is found to be a practical way in the LBM to enlarge the time step, so that the convergence rate can be speeded up.

ACKNOWLEDGMENTS

The authors thank Dr. Xiaoyi He for his useful and instructive discussion during this work.

REFERENCES

1. F. Nannelli and S. Succi, The lattice Boltzmann equation on irregular lattices, *J. Statist. Phys.* **68**(3/4):401 (1992).
2. S. Succi, G. Amati, and R. Benzi, Challenges in lattice Boltzmann computing, *J. Statist. Phys.* **81**:5 (1995).
3. H. Chen, Volumetric formulation of the lattice Boltzmann method for fluid dynamics: Basic concept, *Phys. Rev. E* **58**:3955 (1998).
4. X. He, L.-S. Luo, and M. Dembo, Some progress in lattice Boltzmann method, Part I. Non-uniform mesh grids, *J. Comput. Phys.* **129**:357 (1996).
5. O. Filippova and D. Hanel, Grid refinement for Lattice-BGK models, *J. Comput. Phys.* **147**:219 (1998).
6. O. Filippova and D. Hanel, Acceleration of Lattice-BGK schemes with grid refinement, *J. Comput. Phys.* **165**:407 (2000).
7. G. Peng, H. Xi, and C. Duncan, Lattice Boltzmann method on irregular meshes, *Phys. Rev. E* **58**:4124 (1998).
8. G. Peng, H. Xi, and C. Duncan, Finite volume scheme for the lattice Boltzmann method on unstructured meshes, *Phys. Rev. E* **59**:4675 (1999).

9. H. Xi, G. Peng, and S. Chou, Finite-volume lattice Boltzmann method, *Phys. Rev. E* **59**:6202 (1999).
10. H. Xi, G. Peng, and S. Chou, Finite-volume lattice Boltzmann schemes in two and three dimensions, *Phys. Rev. E* **60**:3380 (1999).
11. C. Hirsch, *Numerical Computation of Internal and External Flows, Vol. I: Fundamentals of Numerical Discretization* (Wiley, Chichester, 1988).
12. G. Peng, H. Xi, and S. Chou, On boundary conditions in the finite volume lattice Boltzmann method on unstructured meshes, *Int. J. Mod. Phys. C* **10**(6):1003 (1999).
13. H. Grad, On the kinetic theory of rarefied gases, *Commun. Pure Appl. Math.* **2**:331 (1949).
14. Q. Zou and X. He, On pressure and velocity boundary conditions for the lattice Boltzmann BGK model, *Phys. Fluids* **9**:1591 (1997).
15. M. Napolitano and P. Orlandi, Laminar Flow in a Complex Geometry: A Comparison, *Int. J. Numer. Methods Fluids* **5**:667 (1985).
16. U. Ghia, K. N. Ghia, and C. T. Shin, High-Re solutions for incompressible flow using the Navier–Stokes equations and a multigrid method, *J. Comput. Phys.* **48**:387 (1982).